Article

Thermal Assessment of a Micro Fibrous Fischer Tropsch Fixed Bed Reactor Using Computational Fluid Dynamics

Aya E. Abusrafa [1,2,†], **Mohamed S. Challiwala** [1,2,3,†], **Benjamin A. Wilhite** [2] **and Nimir O. Elbashir** [1,3,*]

[1]   Chemical Engineering & Petroleum Engineering Program, Texas A&M University at Qatar, Education City, Doha 23874, Qatar; aya.abusrafa@qatar.tamu.edu (A.E.A.); m.challiwala@tamu.edu (M.S.C.)
[2]   Artie McFerrin Department of Chemical Engineering, Texas A&M University, College Station, TX 77840, USA; benjaminwilhite@exchange.tamu.edu
[3]   Gas and Fuels Research Center, Texas A&M Engineering Experiment Station, College Station, TX 77843, USA
*   Correspondence: nelbashir@tamu.edu
†   First and Second authors have contributed equally.

Abstract: A two-dimensional (2D) Computational Fluid Dynamics (CFD) scale-up model of the Fischer Tropsch reactor was developed to thermally compare the Microfibrous-Entrapped-Cobalt-Catalyst (MFECC) and the conventional Packed Bed Reactor (PBR). The model implements an advanced predictive detailed kinetic model to study the effect of a thermal runaway on C_{5+} hydrocarbon product selectivity. Results demonstrate the superior capability of the MFECC bed in mitigating hotspot formation due to its ultra-high thermal conductivity. Furthermore, a process intensification study for radial scale-up of the reactor bed from 15 mm internal diameter (ID) to 102 mm ID demonstrated that large tube diameters in PBR lead to temperature runaway >200 K corresponding to >90% CO conversion at 100% methane selectivity, which is highly undesirable. While the MFECC bed hotspot temperature corresponded to <10 K at >30% CO conversion, attributing to significantly high thermal conductivity of the MFECC bed. Moreover, a noticeable improvement in C_{5+} hydrocarbon selectivity >70% was observed in the MFECC bed in contrast to a significantly low number for the PBR (<5%).

Keywords: Fischer Tropsch; syngas; CFD; entrapped cobalt catalyst; thermal management

1. Introduction

Fischer Tropsch (FT) synthesis, central to many gas-to-liquid (GTL) processes, is a process in which synthesis gas (or syngas, i.e., a mixture of H_2 and CO) is converted to a variety of hydrocarbon products including paraffin, olefins, and value-added chemicals [1–6]. FT synthesis is a highly exothermic reaction (the total heat released per mole of CO consumed is from 140 kJ/mol to 160 kJ/mol), and therefore, efficient heat removal is one of the main considerations while designing commercial-scale FT reactors [7,8]. Uncontrollable temperature gradients lead to the formation of local hotspots, and in some cases, unstable temperature runaways, which promote methane formation, lower the selectivity of the desired hydrocarbon products and lead to fast catalyst deactivation [2,6,9–16].

Currently, there are two modes for FT synthesis operation; High-Temperature Fischer Tropsch (HTFT) and Low-Temperature Fischer Tropsch (LTFT) [17,18]. The LTFT process is a three-phase process (gas-liquid-solid) and typically operates at temperatures ranging from 473 K to 513 K and utilizes cobalt-based catalysts to produce heavy hydrocarbons such as diesel and wax [4,19,20]. On the other hand, the HTFT process mainly involves two phases (gas-solid) [21], which operates at temperatures from 593 K to 623 K, and utilizes fused iron-based catalysts to produce lighter hydrocarbons such as

olefins, oxygenates and gasoline [22]. HTFT operation is mainly conducted in fluidized bed reactors (FBR), while LTFT is applied in multi-tubular fixed bed (or packed bed reactors (PBR)), and Slurry Bubble Column reactors (SR). PBR has several advantages and is most often used in commercial applications [21]. This is due to the simple operation, high catalyst holdup, easy scale-up from a single tube to an industrial size multi-tubular reactor and shutdown robustness of the PBR compared to SBR and FBR [23,24]. Moreover, the separation of the Catalyst from the liquid product is not required in PBR. The liquid products in PBR trickle down through the reactor bed and are separated from the exit gas using a knock out vessel [7]. This imposes significant reductions in the operational costs of the process. On the other hand, due to the pressure drop limitations in PBR, particles relatively larger than 1 mm are utilized. These requirements lead to mass transfer limitations, as well as hotspot formations, that can negatively affect the product selectivity [25]. Therefore, to achieve higher productivity within the reactor bed, more active catalysts with higher thermal conductivity are needed, hence increasing the amount of heat released during the reaction. This would result in high radial and axial temperature gradients along the catalytic bed. This in return will lead to temperature runaways and loss of selectivity due to the poor effective thermal conductivity of the PBR [26,27]. For this reason, such types of reactors utilize several hundred to around ten thousand small diameter tubes (from about 20 mm to 50 mm) to facilitate heat removal [21]. The short distance between the catalyst particles and the tube walls provides more efficient heat transfer from the catalytic bed to the cooling medium. Additionally, the single-pass conversion in PBR is typically kept at 50% or lower to avoid temperature runaways and hotspot formation [28]. Therefore, a key factor to optimal FT performance in PBR is the efficient heat removal from the reactor bed to the cooling media.

To overcome the heat transfer limitations associated with PBR, a novel catalytic configuration consisting of thin copper microfibrous structures that provide a holder for the catalyst particles has been developed by Tatarchuk et al. [29,30]. Microfibers catalysts (MFEC) made of sintered micron-sized metal, glass or polymer fibers with small catalyst particles entrapped inside have also been reported [29,31]. These catalysts have been utilized in several studies to mitigate bed channeling, improve electrical conductivity in fuel cells and remove harmful airborne contaminants in air filtration systems [29,32–34]. The Microfibrous Entrapped Cobalt-based Catalytic Structure (MFECC) is produced by entrapping small cobalt particles in a porous metal sheet (made of copper) of interlocking microfibers [9]. Due to the micron-sized fibers of the microfibrous Catalyst, a large geometric surface area is offered, which dramatically enhances the thermal conductivity of the reactor bed compared to conventional PBR [29]. The high thermal conductivity and low thermal resistance of this catalytic matrix provide a significant improvement in temperature control compared to conventional PBR. Improved temperature control leads to longer catalyst lifetime and activity. The improved heat characteristics provided using MFECC structures allows the use of smaller catalyst particles with diameters ranging from 0.01 mm to 0.1 mm to eliminate mass transport resistances [29]. This provides better utilization of the Catalyst, and thus, higher productivity is achieved. Furthermore, MFECC provides a higher void fraction that results in a reduction of pressure drops compared to conventional PBR [29]. An experimental study of thermal conductivity of a conventional PBR catalyst and MFECC catalyst was conducted by Sheng et al. [29]. The study revealed that the effective radial thermal conductivity of MFECC was 56 times higher than that of PBR diluted with fresh alumina, while the wall heat transfer coefficient was ten times higher than that of the alumina PBR. Another study done by Kalluri et al. investigated the effect of bed porosity on the transport resistances for MFEC structures and diluted PBR [32]. They found that decreasing the bed void of the PBR only improved the flow disturbances and radial dispersion to a small extent. In contrast, the high void of the microfibrous structures promoted radial dispersion, which in turn led to more uniform radial concentration profiles and reduced flow disturbances.

To date, the implementation of this novel FT reactor technology has been limited to the laboratory scale. Several aspects still need to be addressed before the commercialization of MFECC reactor beds. The most important aspect is the scale-up to larger sized reactors to study the hydrodynamics and reactor performance under conditions used in the industry, which cannot be achieved experimentally.

The latter, however, can be done by applying Computational Fluid Dynamics (CFD) to represent the fluid behavior inside the reactor bed accurately. In our previous work, a two-dimensional (2D) model was developed to study the effect of using a non-conventional Supercritical Fluid (SCF) reaction media on the heat management characteristics of the bed [3,5]. Moreover, Challiwala et al. developed a 2D pseudo-homogenous model of an MFECC bed and conventional PBR using a simple kinetic model for a cobalt-based catalyst [9]. They analyzed the performance of the MFECC bed and PBR in terms of heat management and CO conversion at the various process and design parameters (inlet temperature, inlet flowrate, tube diameter). This study aims to extend on their works [3,5,9] and develop a 2D model of an FT fixed bed reactor (FB) in COMSOL® Multiphysics v5.3a utilizing a detailed kinetic model for a cobalt-based catalyst for two systems; non-conventional MFECC bed and conventional PBR, both operating under gas-phase conditions (GP-FT). The model is used to study the effect of the thermal performance of both the reactor systems on conversion levels and hydrocarbon product selectivity. Moreover, the potential of scaling-up the reactor tube diameter above typical industrial diameter (more than 102 mm internal diameter (ID)) was studied as a starting point to improve the performance of conventional FT technologies.

2. Materials and Methods

The fixed bed reactor was developed in 2D axisymmetric space via COMSOL® Multiphysics v5.3a [Multiphysics, 1998 #508]. The model geometry comprises three zones of pre-packing, catalytic bed and post-packing, respectively, as shown in Figure 1. For model validation purposes, the reactor dimensions in the CFD model were specified based on the geometry of the reactor used to conduct the FT experiments. Two-dimensional correlations were used in this modeling study for momentum, heat and mass transfer to account for the variation of concentration and temperature in the radial and axial directions. This is because, for larger tube diameters (scaling-up) [35], higher radial temperature gradients are expected, which will have a direct effect on the overall performance of the reactor bed. Since the main goal of this modeling work is to study the effect of heat generation on the reactor bed performance, including conversion and hydrocarbon product selectivity at larger tube diameters (up to 102 mm), a 2D modeling approach was chosen [35].

The fixed bed reactor developed in this work was modeled as a pseudo-homogeneous model. This assumption indicates that the interfacial mass and heat resistances occurring between the solid phase and the fluid phase are neglected. This implies that the catalyst effectiveness factor (the ratio of the overall reaction rate in the pellet to the surface reaction rate for a specific component) is equal to 1. Sheng et al. [29,30] calculated the effectiveness factor for 0.162 mm particle size to study the effect of intraparticle diffusion. Results showed that the effectiveness factor was relatively high (0.87); therefore, in this modeling study the internal diffusion effects were neglected. The fluid flow was assumed to be a single-phase flow; however, the presence of the liquid was considered by calculating the liquid physical properties (heat capacity, thermal conductivity, viscosity, diffusivity, density) of the hydrocarbon cuts which exist in the liquid and gas phase (GP).

Modeling and simulation of the FT reactor bed require a simultaneous solution of momentum, mass and energy balance equations in the three zones specified earlier: pre-packing, catalytic bed and post-packing. The entire operation is considered to be at steady state. The reactants CO and H_2 enter the reactor to the pre-packing zone and exit the reactor from the post-packing region, which is inert and non-catalytic. It is assumed that the reaction only takes place in the catalytic bed over 15% Co/Al_2O_3 catalyst particles of identical sphericity ($\emptyset = 1$). Additional assumptions and more details are stated in each part of the model development section.
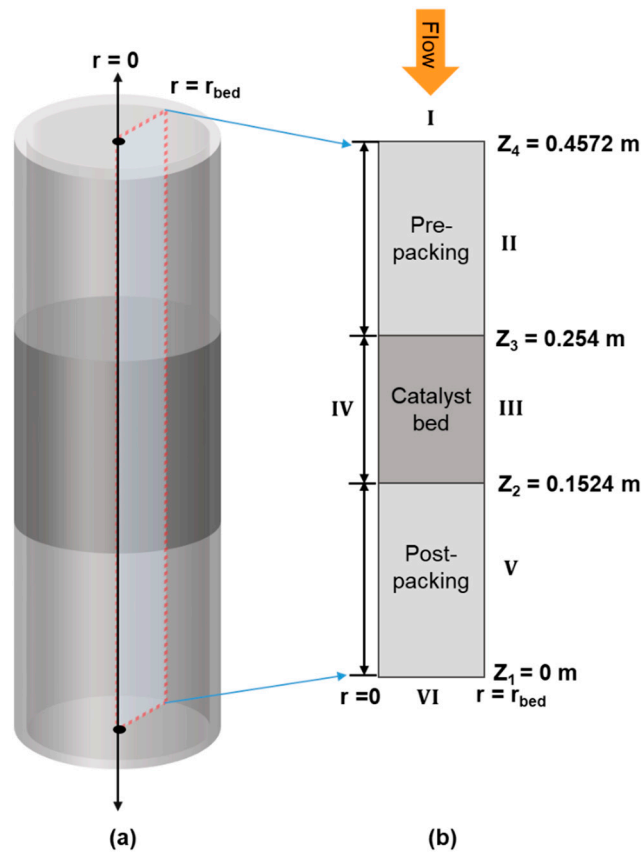
Figure 1. (**a**) Three-dimensional model and (**b**) 2D-axisymmetric cut section of the Fischer Tropsch (FT) reactor bed model cylindrical geometry.

2.1. Momentum Transport Expressions

To model fluid flow in porous media, a built-in module in COMSOL® Multiphysics called "Brinkman Equation," was adopted Equation (1). The Brinkman physics module is used to compute the fluid velocity and pressure field in single-phase flow in porous media in the laminar flow regime. This mathematical model extends Darcy's law to account for dissipation in kinetic energy due to shear stress, similar to the Naiver stokes equation [36]. This physics module comprises two main terms; the Forchheimer drag term and the convective term. The convective terms take into account the effect of inertial and viscous forces on the fluid flow through the porous medium. The Forchheimer drag term accounts for the inertial drag effects that occur in fast flows (Reynold number (*Re*) greater than unity) [37]. Considering slow flow regimes where *Re* is less than unity, the Forchheimer drag contributions are neglected. The 2D single-phase fluid flow through the PBR is described in terms of the velocity (*u*) and pressure fields (*p*), which are computed via solving the momentum equation and continuity equation (Equation (1) and Equation (2), respectively) simultaneously along with boundary conditions (Equation (3)) pertaining to (i) radial symmetry, (ii) no-slip condition at the wall, (iii) inlet mass flow, (iv) outlet pressure. The changes in volumetric gas flow rates of the reacting species during the FT reaction results in variations in the fluid density; therefore, a compressible flow formulation of the continuity equation is used. When a compressible flow is modelled using the Brinkman equation, the Mach number must be below 0.3. This condition is fulfilled in this case study.

$$\frac{1}{\epsilon_{bed}}\rho_f(\boldsymbol{u}\cdot\nabla)\boldsymbol{u}\frac{1}{\epsilon_{bed}} = \nabla\cdot\left[-p\boldsymbol{I} + \varphi_f\frac{1}{\epsilon_{bed}}\left(\nabla\boldsymbol{u} + (\nabla\boldsymbol{u})^T\right) - \frac{2}{3}\varphi_f\frac{1}{\epsilon_{bed}}(\nabla\cdot\boldsymbol{u})\boldsymbol{I}\right] - \left(\frac{\varphi_f}{\kappa_{bed}} + \beta_f|\boldsymbol{u}|\right)\boldsymbol{u} \quad (1)$$

$$\nabla(\rho_f\mathbf{u}) = 0 \quad (2)$$

$$\boldsymbol{u} = 0 \ @ \ r = r_{\text{bed}}, q_m = q_{m,o} \ @ \ z = z_4, \ \boldsymbol{p} = p_e \ @z = z_1 \tag{3}$$

where, φ_f is the dynamic viscosity of the fluid, ϵ_{bed} is the porosity, ρ_f is the density of the fluid, κ_{bed} is the permeability of the porous media, β_f is the Forchheimer drag coefficient, r is the radius of the reactor bed, q_m is the mass flow rate and z is the height of the reactor bed (cartesian coordinate). A constant porosity of 0.626 was chosen for the MFECC bed, while 0.36 was chosen for the PBR per the catalyst specifications reported by Sheng et al. [29,30].
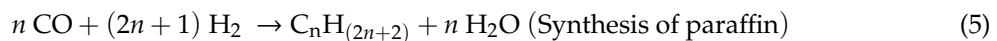
The permeability of the porous medium was calculated using the modified Ergun equation [38]:

$$\frac{1}{\kappa_{\text{bed}}} = \frac{150(1 - \epsilon_{\text{bed}})^2}{d_{\text{p}}^2 \epsilon_{\text{bed}}{}^2} + \frac{1.75 \rho_f u (1 - \epsilon_{\text{bed}})}{d_{\text{p}} \varphi_f \epsilon_{\text{bed}}{}^3} \tag{4}$$

where d_{p} is the particle diameter.

2.2. Mass Transport Expressions

Mass conservation equations for the pseudo homogenous reaction (assuming catalyst effectiveness as unity) is defined for each component of the reaction mixture of the following FT reactions:

$$n \, CO + (2n + 1) \, H_2 \ \rightarrow C_nH_{(2n+2)} + n \, H_2O \text{ (Synthesis of paraffin)} \tag{5}$$

$$n \, CO + 2n \, H_2 \ \rightarrow C_nH_{2n} + n \, H_2O \ \text{ (Synthesis of olefins)} \tag{6}$$
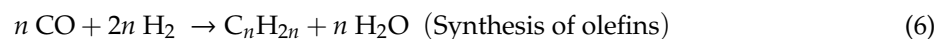
Components considered in the system are N_2, CO, H_2, H_2O, CH_4, CH_o and CH_p. N_2 was set as the mass constraint component since it is a non-reacting species. The hydrocarbon components CH_o and CH_p are the summation of olefins and paraffin products, respectively. This was done for C_1, C_2, C_3, . . . , C_{15} components. The C_{15} to C_{22} hydrocarbons are lumped into one component represented by a paraffinic compound $C_{19}H_{40}$, while the higher weight hydrocarbons C_{22+} are represented by the paraffinic component $C_{22}H_{40}$. It is important to note that this study considers a cobalt-based catalyst where the rate of water-gas shift reaction is assumed to be negligible. Therefore, selectivity calculations of CO_2 have not been considered in this modeling study.

The local mass balance for species i (N_2, CO, H_2, H_2O, CH_4, CH_o, and CH_p) was described by Equation (7) using a built-in physics module "Transport of concentrated species." This physics accounts for mass transport through convection and diffusion in the axial and radial directions. The equation provided in COMSOL® Multiphysics for transport mechanism is as follows:

$$\nabla j_i + \rho_f (\boldsymbol{u} \cdot \nabla) w_i = r_i \tag{7}$$

where w_i is the mass fraction of species i, j_i is the mass flux relative to the mass averaged velocity of species i and r_i is the reaction rate representing production or consumption of species i.

The diffusion model selected in this case was the Maxwell Stefan diffusion model, where the relative mass flux vector is calculated using Equation (8):

$$j_i = - \rho_f w_i \sum D_{ik} d_k \tag{8}$$

where D_{ik} represents the binary diffusion coefficient and d_k is the diffusional driving force acting on species k defined as follows:

$$d_k = \nabla x_k + \frac{1}{p}[(x_k - w_k)\nabla p] \tag{9}$$

where x_k is the mole fraction is species k.

Equations (7)–(9) are solved using appropriate boundary conditions corresponding to (i) axial symmetry, (ii) no-flux at the wall and (iii) inlet composition:

$$\frac{\partial w_i}{\partial r} = 0 \; @ \; r = r_{\text{bed}}, \; w_i = w_{i,o} \; @ \; z = z_4 \qquad (10)$$

The binary diffusivities D_{ik} in the Maxwell-Stefan diffusion model are estimated using Fickian diffusivities with an empirical correlation proposed by Fuller et al. [39]:

$$D_{ik} = \frac{\sqrt{\frac{1}{M_i} + \frac{1}{M_k}}}{p\left(v_{c,i}^{\frac{1}{3}} + v_{c,k}^{\frac{1}{3}}\right)^2} \times 10^{-7} \qquad (11)$$

where M_n represents the mean molar mass and v_c represents the molar volume for species i and k. The molar volume of the representative paraffin and olefin components CH_o and CH_p are calculated based on the ASF product distribution. A correlation based on the molar weight average sum using the molar volumes of the individual hydrocarbon species is used. The molar volumes of H_2O, CO, H_2, N_2 and CH_4 used in this model are: (12.7, 18.9, 7.07, 17.9 and 37.9) $\frac{\text{cm}^3}{\text{mol}}$, respectively.

2.3. Heat Transport Expressions

Energy balance within the 2D reactor domain was considered to account for the transport of heat through convection, conduction and thermal dispersion. Radiative heat transport was neglected in this case. Balance equations were solved using the simplified "Heat transfer in porous media physics" Equation (12):

$$\rho_f C_p \boldsymbol{u} \cdot \nabla T - \nabla(k_{\text{eff}} \nabla T) = (-\Delta H_{\text{rxn}}) R_{\text{CO}} \qquad (12)$$

where T is the temperature inside the reactor bed, C_p is the heat capacity of the fluid mixture, k_{eff} is the effective thermal conductivity of the reactor bed, R_{CO} is the rate of consumption of carbon monoxide and ΔH_{rxn} is the heat of the reaction per mole of CO consumed.

The reaction enthalpy $(-\Delta H_{\text{rxn}})$ is an important parameter that determines the amount of heat released during the FT reaction. Previous modeling studies reported values of $(-\Delta H_{\text{rxn}})$ ranging from 150 kJ/mol to 165 kJ/mol to represent the FT reaction enthalpy [9,21,30,40,41]. Its value mainly depends on the hydrocarbon product selectivity. The $-\Delta H_{\text{rxn}}$. value used in this study was 152 kJ/mol.

The effective thermal conductivity of the bed was calculated using a volume-based average model to account for both the solid matrix and the fluid properties:

$$k_{\text{eff}} = \epsilon_{\text{bed}} k_s + (1 - \epsilon_{\text{bed}}) k_f \qquad (13)$$

where k_s is the thermal conductivity of the catalyst bed and k_f is the thermal conductivity of the fluid mixture.

Equation (12) was solved along with boundary conditions corresponding to (i) radial symmetry, (ii) external cooling (heat transfer between the reactor and a constant temperature cooling medium), (iii) inlet temperature and (iv) open outflow:

$$k_{\text{er}} \frac{\partial T}{\partial r} = U_{\text{overall}}(T_c - T) @ \; r = r_{\text{bed}}, T = T_o @ \; z = z_3, \; \frac{\partial T}{\partial z} = 0 \; @ \; z = 0 \qquad (14)$$

The overall heat transfer coefficient (U_{overall}) represents the overall heat transmittance from the reactor bed to the vicinity of the wall. The latter is defined using the following correlation suggested by Mamonov et al. [42]:

$$U_{\text{overall}} = \left(\frac{d_t}{8k_{\text{er}}} + \frac{1}{h_{\text{wall}}} + \frac{d_w}{k_w} + \frac{1}{h_{\text{w,ext}}} \right) \qquad (15)$$

where d_t is the inner tube diameter, k_{er} is the effective radial heat coefficient of the catalyst bed, $h_{w,int}$ is the radial heat transfer coefficient near the wall, d_w is the wall thickness, k_w is the thermal conductivity of the wall and $h_{w,ext}$ is the heat transfer coefficient from the tube wall to the cooling liquid. Values for k_w and $h_{w,ext}$ were taken from Mamonov et al. [42].

(1)　Radial Heat Transfer Coefficient at the Wall

The effective radial heat transfer coefficient at the wall h_{wall} is one of the main parameters that determine the rate of heat transfer in PBR. This parameter quantifies the increase in heat transfer resistance near the wall of the reactor bed. Several correlations to properly estimate the h_{wall} value has been proposed in the literature [43–51]. Specchia and Baldi proposed a two-parameter correlation that has shown to satisfactorily predict the h_{wall} value in PBR with different particle geometries [21]. This was used in the present work:

$$h_{wall} = h_{wall,o} + h_{wall,g} \tag{16}$$

$$h_{wall,o} = \frac{k_f}{d_p}\left(2\epsilon_{bed} + \frac{1 - \epsilon_{bed}}{\frac{k_f}{k_s} \times \gamma_w + \varphi_w}\right) \tag{17}$$

$$h_{wall,g} = \frac{k_f}{d_p} \times 0.0835 \times Re^{0.91} \tag{18}$$

where γ_w and φ_w are dimensionless parameters, Re represents the Reynold numbers and $h_{wall,o}$ represents the stagnant/conductive contribution while $h_{wall, g}$ represents the convective contribution.

The dimensionless parameters γ_w and φ_w in Equation (17) are dependent on the geometry of the contact surface between the particle and the wall. For spherical particles, the parameters are defined as $(\gamma_w = \frac{1}{3}, \varphi_w = 0.0024 \times \left(\frac{d_t}{d_p}\right)^{1.58})$ [47].

(2)　Effective Radial Thermal Conductivity

The effective radial thermal conductivity is one of the main parameters that determine the rate of heat transfer in PBR; the parameter effecting heat transfer in PBR is the radial effective thermal conductivity k_{rad}. A two-parameter correlation that adequately predicts the effective radial heat transfer coefficient in PBR was taken from Specchia and Baldi [46]:

$$k_{rad} = k_{rad,o} + k_{rad,g} \tag{19}$$

$$k_{rad,o} = \left(\epsilon_{bed} + \frac{\beta(1 - \epsilon_{bed})}{\varphi + \frac{k_f}{k_s} \times \gamma}\right)k_f \tag{20}$$

$$k_{rad,g} = \frac{Re_{pa}Pr}{8.65\left(1 + 19.4 \times \frac{d_p}{d_t}^2\right)}k_f \tag{21}$$

where Pr represents the Prandtl number, β, γ and φ represent the ratios between characteristic lengths and the particle diameter (the particles are assumed to be spheres) and $k_{rad,o}$ represents the static/conduction contribution while $k_{rad,g}$ represents the convective contribution.

Kunii and Smith reported that for spherical particles $\beta = 1$ for almost all packed beds, $\gamma = \frac{2}{3}$ and $\varphi = 0.22(\epsilon_{bed})^2$ based on fitting of experimental data for $k_{rad,o}$ [52].

2.4. Kinetics

The rate of CO disappearance is calculated using the Yates and Satterfield (YS) kinetic model, which has been commonly used in previous modeling studies [21,25,53–57]:

$$-r_{CO}{}^{YS} = \frac{k\, p_{H_2} p_{CO}}{(1 + a\, p_{CO})^2} \tag{22}$$

$$k = A_k\, exp\left(-\frac{E_k}{RT}\right) \tag{23}$$

$$a = A_a\, exp\left(-\frac{E_a}{RT}\right) \tag{24}$$

where p_{CO}, and p_{H_2} are the partial pressures of CO and H_2, k and a are the kinetic rate constants, A_k and A_a are the pre-exponential factors and E_k and E_a are the activation energies for CO consumption.

The product selectivity for CH_4 and C_{2+} hydrocarbons is calculated using a kinetic model by Ma et al. [58] and a detailed kinetic model of Todic et al. [59], respectively. The Ma kinetic model for CH_4 formation was proven to provide a good prediction of CH_4 selectivity [55], while the detailed kinetic model developed based on the carbide mechanism showed a good prediction of the hydrocarbon product distribution [59].

The rate of formation of CH_4 by the following expression [58]:

$$r_{CH_4}{}^{Ma} = \frac{k_M p_{CO}{}^{a_M} p_{H_2}{}^{b_M}}{1 + m_M \frac{p_{H_2O}}{p_{H_2}}} \tag{25}$$

$$k_M = A_M\, exp\left(-\frac{E_M}{RT}\right) \tag{26}$$

where k_M is the rate constant, m_M is the water effect coefficient, a_M is the reaction order of CO, b_M is the reaction order of H_2, A_M is the pre-exponential factor and E_M is the activation energy for CH_4 formation.

The rate of formation of the C_{2+} hydrocarbons from the detailed kinetic model by Todic et al. [59] performance as follows:

$$r_{C_2H_4}{}^{Prod} = k_{6E,0}\, e^{2c} \sqrt{K_7 p_{H_2}} \alpha_1 \alpha_2 [S] \tag{27}$$

$$r_{C_nH_{2n+2}}{}^{Prod} = k_5 K_7{}^{0.5} p_{H_2}{}^{1.5} \alpha_1 \alpha_2 \prod_{i=3}^{n} \alpha_i [S]\ n \geq 2 \tag{28}$$

$$r_{C_nH_{2n}}{}^{Prod} = k_{6,0}\, e^{cn} \sqrt{K_7 p_{H_2}} \alpha_1 \alpha_2 \prod_{i=3}^{n} \alpha_i [S]\ n \geq 3 \tag{29}$$

where the ks represent the kinetic rate constants, Ks represent the equilibrium constants, α_n are the chain growth probabilities and $[S]$ is the fraction of vacant sites.

The chain growth probabilities dependent on the carbon number are calculated using the following expressions:

$$\alpha_1 = \frac{k_1 p_{co}}{k_{5m} p_{H_2} + k_1 p_{co}} \tag{30}$$

$$\alpha_2 = \frac{k_1 p_{co}}{k_5 p_{H_2} + k_{6,0}\, e^{2c} + k_1 p_{co}} \tag{31}$$

$$\alpha_n = \frac{k_1 p_{co}}{k_5 p_{H_2} + k_{6,0}\, e^{cn} + k_1 p_{co}}\ n > 2 \tag{32}$$

The fraction of vacant sites is calculated as follows:

$$[S] = 1/\left\{1 + \sqrt{K_7 p_{H_2}} + \sqrt{K_7 p_{H_2}}\left(1 + \frac{1}{K_4} + \frac{1}{P_{H_2} K_3 K_4} + \frac{1}{K_2 K_3 K_4}\frac{p_{H_2O}}{p_{H_2}}\right)(\alpha_1 + \alpha_1\alpha_2 + \alpha_1\alpha_2\sum_{i=3}^{n}\prod_{j=3}^{i}\alpha_j\right\} \quad (33)$$

The kinetic parameters in the detailed kinetic model, YS model, and the Ma kinetic model were estimated by Todic et al. [59] and Stamenic et al. [55] using experimental data with 0.48%Re 25%Co/Al_2O_3 catalyst.

In this work, a hybrid kinetic model adopted by Stamenic et al. [55] and Bukur et al. [56] was used. In their works, they coupled the YS model, the Ma model and a detailed kinetic model based on the CO insertion mechanism. In this case study, the reaction rates for CO, H_2, H_2O, CH_p (n-paraffin) and CH_o (1-olefins) was defined by coupling the YS kinetics for CO consumption, Ma et al. kinetics for CH_4 formation and the detailed kinetic model of Todic et al. for C_{2+} hydrocarbon formation based on the carbide mechanism. A normalization procedure was followed to obtain atomic balances for C, O and H. The procedure was done described below.

The rate of consumption of CO excluding methane from the detailed kinetic model (rate of C_{2+} formation from the model by Todic et al.) can be calculated based on the reaction stoichiometry as:

$$(-r_{CO})_{C_{2+}}^{Prod} = \sum_{n=2}^{n} n\left(r_{C_nH_{2n+2}}^{Prod} + r_{C_nH_{2n}}^{Prod}\right) \quad (34)$$

The rate of CO consumption excluding methane from the YS model (rate of C_{2+} formation from YS model) is calculated as:

$$(-r_{CO})_{C_{2+}}^{YS} = \left(-r_{CO}^{YS}\right) - \left(r_{CH_4}^{Ma}\right) \quad (35)$$

The normalized rates of formation of C_{2+} hydrocarbons are obtained as follows:

$$r_{C_nH_{2n+2}} = r_{C_nH_{2n+2}}^{Prod} \times \frac{(-r_{CO})_{C_{2+}}^{Prod}}{(-r_{CO})_{C_{2+}}^{YS}} \quad n \geq 2 \quad (36)$$

$$r_{C_nH_{2n}} = r_{C_nH_{2n}}^{Prod} \times \frac{(-r_{CO})_{C_{2+}}^{Prod}}{(-r_{CO})_{C_{2+}}^{YS}} \quad n \geq 2 \quad (37)$$

From the stoichiometry, the H_2 formation rate is calculated using the individual product formation rates of the hydrocarbon species as:

$$-r_{H_2} = 3r_{CH_4}^{Ma} + \sum_{n=2}^{n}\left[(2n+1)r_{C_nH_{2n+2}} + 2nr_{C_nH_{2n}}\right] \quad (38)$$

The rate of H_2O formation is equal to the rate of CO consumption based on the reaction stoichiometry:

$$r_{H_2O} = -r_{CO}^{YS} \quad (39)$$

3. Results

3.1. Comparison of Model Predictions with Experimental Data

The developed model was validated with experimental data reported by Sheng et al. [29,30] to test its robustness under different experimental conditions. Sheng et al. reported two experiments to compare between the PBR and MFECC beds under GP conditions [30]. The experiment was conducted in a stainless-steel tubular reactor with a wall thickness of 2 mm and 15 mm ID. The total height of the reactor bed was 457.2 mm compromising of a 203.2 mm pre-packing zone, a 101.6 mm catalyst bed and

152.4 mm post-packing zone. The MFECC bed consisted of $\varphi = 37.4\%$ (30% (15% Co/Al$_2$O$_3$) and 7.4% copper fibers) and $\epsilon_{bed} = 62.6\%$. The PBR was diluted to the same catalyst density as the MFECC bed with fresh alumina of different particle sizes. The overall bed space in the PBR comprised $\varphi = 65\%$ (30% (15%Co/Al$_2$O$_3$) and 34% fresh alumina) and $\epsilon_{bed} = 36\%$. The average particle size of the Catalyst in the reactor bed was 0.149 mm to 0.177 mm.

The experimental results were obtained by varying the inlet temperature over a range from 498.15 K to 528.15 K at 2 MPa pressure and syngas molar ratio (H$_2$/CO) of 2:1 at a constant Gas Space Velocity (GHSV) of 5000 h^{-1}. In all simulation runs, the parameters (inlet temperature, pressure, GHSV and H$_2$/CO ratio) were kept identical to those used in the experimental study by Sheng et al. [29,30]. A particle diameter of 0.162 mm was used in the simulation to represent the average particle size of 0.149 mm to 0.177 mm used in the experiments, as reported by Sheng et al. [30].

Four sets of results were used to validate the model with the experimental study, including CO conversion, maximum temperature deviation from the centerline to the reactor wall ($T_{max} - T_{wall}$), CH$_4$ selectivity and C$_{5+}$ selectivity. The simulation results for the MFECC bed demonstrated a clear agreement with the experimental predictions for CO conversion, ($T_{max} - T_{wall}$), CH$_4$ selectivity and C$_{5+}$ selectivity, as shown in Table 1. For the PBR case, the CO conversions from the modeling results consistently match with the experimentally-obtained PBR results under all conditions, as shown in Table 2. Moreover, the ($T_{max} - T_{wall}$), CH$_4$ selectivity and C$_{5+}$ selectivity also closely match with the experimental results from 498.15 to K 518.15 K. However, at 528.15 K, the deviation between the modeling and the experimental predictions becomes higher. This deviation in model predictions from experimental data could be attributed to the sensitivity of the kinetic parameters that are generated using a ruthenium promoted Catalyst of different loading reported by Stamenic et al. [55] and Todic et al. [55,59]. The lower CH$_4$ selectivity predicted from the model at a high operating temperature (528.15 K) can be due to the fact that at high-temperature methane formation could follow multiple reaction routes on FT sites [60,61]; (1) termination of the chain growth, (2) through intermediates participating in chain propagation and (3) due to hydrogenation of surface carbon. The latter methane formation pathway does not follow the polymerization/chain growth route for FT synthesis. However, the kinetic model used in this modeling study to predict the methane selectivity has not considered the secondary pathway for methane formation, thus the methane selectivity shows greater deviation from the predicted values relative to the experimental data. Additionally, the experiments were conducted using a ruthenium catalyst which has lower methane selectivity compared to conventional cobalt-based catalysts. This also results in a deviation in C$_{5+}$ selectivity compared to the experimentally predicted values. Further analysis of the validation results reveals that the deviation of the reactor wall temperature from the centerline temperature for the PBR is higher and increases at a faster rate than the MFECC bed under all temperature conditions (498.15 K to 528.15 K). However, it can be noted that when the inlet temperature reaches 528.15 K, a drastic increase of the centerline temperature inside the PBR occurs. This rapid ignition of the PBR temperature leads to the formation of a hotspot and a rapid decrease in the catalyst activity. Such an effect is not observed in the MFECC bed due to the high thermal conductivity of the copper fibers, which aids in eliminating the formation of hotspots even at a high operating temperature (528.15 K).

A close comparison between the PBR and MFECC in terms of CO conversion indicates that the MFECC bed provides lower conversions compared to the PBR case for the same reactor temperature. However, the rapid increase in reactor temperature in the PBR, leading to hot spot formation, shifts the product selectivity towards methane and light hydrocarbon products. This effect can be observed in Tables 1 and 2, where the CH$_4$ selectivity is higher while the C$_{5+}$ selectivity is lower for the PBR compared to the MFECC bed under all temperature conditions. Thus, the high conversion levels achieved in the PBR reactors go mostly toward the formation of methane. The results discussed above demonstrate that the developed model is valid and applicable to quantitatively compare the performance of the PBR and MFECC bed in terms of thermal profiles and hydrocarbon product selectivity.

Table 1. $T_{max} - T_{wall}$, CO conversion, CH_4 selectivity, C_{5+} selectivity from the model, and experimental results for the Microfibrous-Entrapped-Cobalt-Catalyst (MFECC) reactor concerning wall temperature at 2 MPa pressure for H_2: CO ratio of 2:1 and 5000 h^{-1} Gas Space Velocity (GHSV).

T_{wall} (K)	$T_{max} - T_{wall}$ (K) Experimental	$T_{max} - T_{wall}$ (K) Model	CO Conversion Experimental	CO Conversion Model	CH_4 Selectivity Experimental	CH_4 Selectivity Model	C_{5+} Selectivity Experimental	C_{5+} Selectivity Model
498.15	0	1.65	17	24.85	13	10.64	82.1	83.23
508.15	2.5	2.59	38.25	38.13	17	13.64	80.1	80.42
518.15	4.8	4.05	51.67	54.24	19	17.49	73.8	76.81
528.15	9.5	6.16	78.75	72	21	22.48	70.2	72.1

Table 2. $T_{max} - T_{wall}$, CO conversion, CH_4 selectivity, C_{5+} selectivity from the model, and experimental results for the Packed Bed Reactor (PBR) reactor concerning the wall temperature at 2 MPa pressure for H_2: CO ratio of 2:1 and 5000 h^{-1} GHSV.

T_{wall} (K)	$T_{max} - T_{wall}$ (K) Experimental	$T_{max} - T_{wall}$ (K) Model	CO Conversion Experimental	CO Conversion Model	CH_4 Selectivity Experimental	CH_4 Selectivity Model	C_{5+} Selectivity Experimental	C_{5+} Selectivity Model
498.15	5.6	6.35	35.71	49.33	15	11.66	79.7	82.28
508.15	9	11.75	53.13	69.08	19	16.3	73.4	75.3
518.15	14.1	21.85	86.81	89.74	30	25.2	50.6	69.55
528.15	69.8	48.4	99.32	92.27	83	43.2	12.4	52.68

3.2. Comparison of Thermal Profiles

The validated 2D model for the PBR and MFECC bed was used to compare the thermal profiles of the two reactor beds using different inlet conditions; inlet temperature and GHSV. First, a side by side comparison of the thermal profiles of the PBR and MFECC bed was done to study the radial and axial temperatures of both reactor beds at 528.15 K, 2 MPa pressure, H_2/CO ratio of 2:1 and a constant GHSV 5000 h^{-1}. Figure 2 shows the temperature profile predicted by the 2D reactor model for both PBR and MFECC bed.
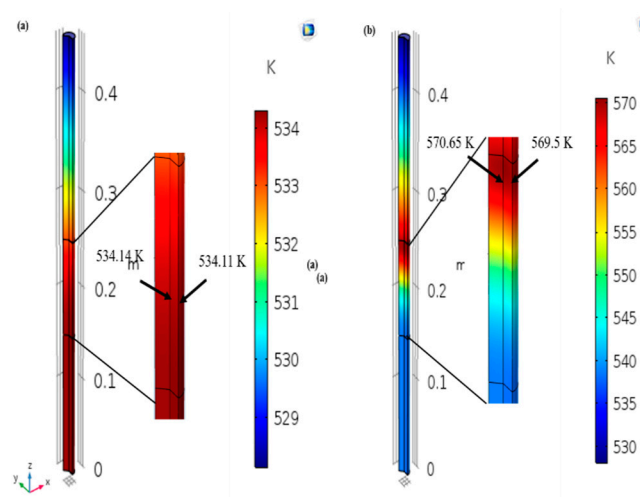
Figure 2. (**a**) Hot spot in MFECC bed and (**b**) Hotspot in PBR under GP conditions for 15 mm ID at 528.15 K, 2 MPa pressure, H_2/CO 2:1 and 5000 h^{-1} GHSV.

As can be seen from Figure 2b, a hotspot is predicted in the PBR at the centerline of the reactor and close to the reactor inlet. Giovanni et al. [40] reported a similar finding for a 2D pseudo homogenous model of a milli-scale fixed FT bed reactor using a Co-based catalyst. The axial temperature deviation for the PB reactor as predicted from the model is around 43 K, and the radial temperature gradient is around 1.15 K. As discussed previously, the temperature deviation predicted from the model for the PBR case at 528.15 K is underpredicted. Therefore, the axial temperature gradient from the experiments conducted by Sheng et al. [30] was even higher—around 70 K. The occurrence of the maximum temperature at the reactor inlet is due to the high partial pressure of the reactants at that location, which results in higher reaction rates. Therefore, heat generation is significantly higher. Moreover, under typical FT conditions, the inlet of the reactor is a region where the liquid is absent since PBR typically operate under trickle bed behavior (the liquid produced during FT trickles down the bed). The latter has negative implications on the heat transfer process inside the PBR reactor. It is worth noting that the PB reactor shows a temperature increase at the pre-packing zone, indicating that the ability of the external cooling on the reactor bed to remove excess heat is extremely insufficient, which leads to a temperature rise at the pre-packing zone and close to the inlet due to thermal diffusion. In the lower part of the reactor, the temperature decreases steadily due to the lower reaction rates in that zone, reducing the amount of heat generated during the reaction. Moreover, the effect of liquid formation at the lower part of the reactor is more prominent (trickle bed behavior), which positively affects the rate of heat transfer within the reactor bed.

The MFECC bed provided better temperature control, and a uniform temperature profile was maintained, as can be seen in Figure 2a. The maximum axial temperature rise in the MFECC bed was only 10 K, and the radial temperature gradient was 0.013 K. This reduction in hot spot formation in the MFECC bed is solely the result of the high thermal conductivity of the MFECC material. Sheng et al. experimentally determined the thermal parameters of the MFECC bed and PBR (effective radial thermal conductivity and wall heat transfer coefficient) [29]. The study reported that the radial effective thermal

conductivity of MFECC was 56 times higher than that of alumina PBR in a stagnant gas, while the inside wall heat transfer coefficient was 10 times higher.

As mentioned previously, the hydrocarbon product distribution in the FT reaction strongly depends on the temperature inside the reactor bed. The hotspot formed in the PBR at 528.15 K resulted in around 100% CO conversion as per experimental results, where most of the conversion goes toward methane formation, as it is favorable at high-temperature conditions (shifting the product selectivity toward lower weight hydrocarbons). Based on the modeling results shown in Table 2, the values of CH_4 and C_{5+} selectivity in the PBR at 528.15 K were 43.2% and 52.68%, respectively. However, as mentioned previously, these values were unpredicted by the model at 528.15 K, and a higher CH_4 selectively, and thus, lower C_{5+} selectivity are expected at such a temperature condition. The experimental values of CH_4 and C_{5+} selectivity in the PBR at 528.15 K were 83% and 12.44%, respectively. For the MFECC, the uniform temperature distribution resulted in higher selectivity toward higher weight hydrocarbon products and lowered CH_4 selectivity. As can be seen from Table 1, the model predictions for CH_4 and C_{5+} selectivity in the MFECC bed at 528.15 K was 22.48% and 72.2%, respectively. The latter findings imply that the MFECC bed provides safe operation under high operational temperatures to achieve high conversions per tube pass in conventional Multi tubular fixed bed reactors/PBR without the risk of selectivity loss.

3.3. Effect of Varying the GHSV

The impact of varying the inlet gas flow rate/GHSV on the heat generation and removal for the MFECC bed and PBR was investigated. The simulations were carried out by varying the GHSV while keeping the other process parameters constant (518.15 K, 2 MPa pressure, H_2/CO 2:1). Figure 3 shows the effect of varying the GHSV on the reactor thermal behavior in terms of maximum temperature rise at the centerline of the reactor. For the PBR, increasing the GHSV from 5000 h^{-1} to 10,000 h^{-1} results in less efficient heat removal, leading the centerline temperature to increase from 566 K to 628 K. This resulted in hotspot formation and temperature runaways. This is due to the poor thermal conductivity of the PBR reactor. For the MFECC bed, the maximum temperature at the centerline of the reactor remains almost constant under all GHSV conditions (5000 h^{-1} to 10,000 h^{-1}) at 534.5 K. Therefore, operating at higher velocities induces very small changes in the thermal behavior of the MFECC bed. The observations in the thermal behavior of both the PBR and MFECC discussed above are also supported by a modeling study conducted by Sheng et al., who conducted a microscale heat transfer comparison between a PBR and an MFECC bed in a stagnant gas and flowing nitrogen gas conditions [62]. They reported that 97.2% of the total heat flux transferred within the MFECC bed was found to be transported by the continuous metal fibers. This demonstrates that the continuous metal fibers were the primary conduction path for the heat transfer inside the MFECC bed. Therefore, it is expected that changing the GHSV would not have a significant effect on the thermal profile inside the MFECC bed. Moreover, they reported the temperature distribution inside the PBR and MFECC bed at two different gas velocities (200 m/s and 500 m/s), and they found the temperature of the flowing nitrogen gas at higher gas velocity decreased significantly in PBR, while in the MFECC bed it did not change much. This finding indicates that increasing the gas velocity inside the MFECC provides stable temperature profiles and efficient heat transfer between the solid/fluid interfaces. On the other hand, increasing the gas velocity in the PBR reactor provides inadequate heat transfer rates between the solid and the fluid interface, which could be the main reason in the formation of local hotspots on catalyst particles inside PBR reactors. This indicates that operating at high gas velocities would have a detrimental effect on heat removal/management inside the PBR reactor.
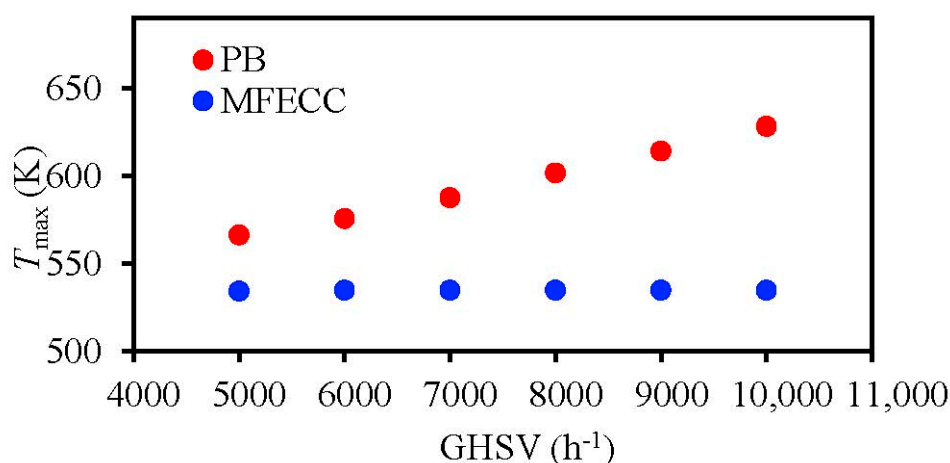
Figure 3. $T_{max} - T_{wall}$ versus GHSV for PBR and MFECC bed at 528.15 K, 2 MPa pressure, H_2: CO ratio 2:1.

Similarly, Figure 4 shows the effect of varying the GHSV on CO conversion. It can be noted that the CO conversion for the PBR case decreases from 93.45% to 83% as the GHSV increases from 5000 h^{-1} to 10,000 h^{-1}. This finding was expected since lower residence times are associated with higher gas velocities. Although the shortening of the residence time results in lower CO conversions, the total amount of syngas converted into hydrocarbons is observed to be higher for higher gas velocities. Therefore, more heat generation per mole of CO consumed is expected at higher GHSV values, which also explains the ascending trend of the centerline temperature with increasing GHSV. A similar trend is observed in the case of the MFECC bed, where the CO conversion decreases from 71.95% to 50.6% as the GHSV increases from 5000 h^{-1} to 10,000 h^{-1}. However, a steeper decrease in CO conversions with increasing GHSV was noted for the MFECC bed. This is mainly due to the high-temperature rise/deviation in the PBR reactor, which was much more prominent than in the MFECC as the GHSV was increased. This effect contributes to higher CO conversions, thus resulting in a slower decreasing rate of CO conversion in PBR. It should be noted that although increasing the GHSV might have negative implications from heat management and CO conversion standpoint, the total hydrocarbons productivity per catalyst mass is higher as the GHSV increases. The MFECC bed has shown to provide near isothermal operation, leading to improved selectivity control even when the gas velocity is increased. This raises the opportunity to achieve higher hydrocarbon productivity per catalyst mass, thus increasing the catalyst utilization.
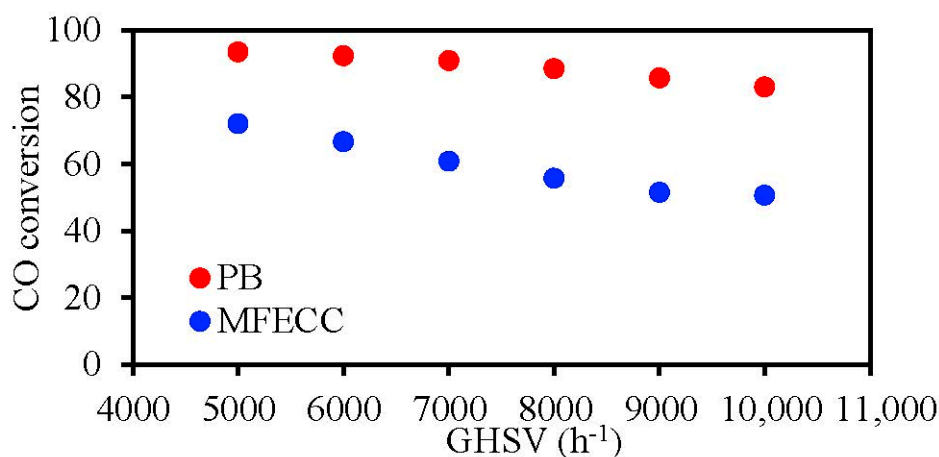

Figure 4. CO conversion versus GHSV for PBR and MFECC bed at 528.15 K, 2 MPa pressure, H_2: CO ratio 2:1.

The performance of the PBR and MFECC bed at different GHSV values was evaluated in terms of the hydrocarbon product selectivity. As mentioned previously, the CO conversions were higher inside the PBR compared to the MFECC under all GHSV conditions. Thus, the total mass productivity of the hydrocarbons (total amount of hydrocarbons produced) is expected to be higher inside the PBR for the same inlet gas velocity, due to the higher CO conversions associated with it. However, on the other hand, the selectivity toward C_{5+} hydrocarbons was significantly lower in PBR than the MFECC as shown in Figure 5. Most importantly, Figure 6 indicates that the selectivity of the most undesired product methane was significantly higher in the PBR reactor because of the relatively high-temperature gradients inside the reactor bed. The CH_4 and C_{5+} selectivity for the PBR was 42.2% and 54.4%, respectively, at 5000 h^{-1} GHSV. However, the CH_4 selectivity in the PBR reactor goes up to 100% at 10,000 h^{-1} GHSV, resulting in 0% selectivity of the C_{5+} hydrocarbons. Therefore, the total productivity of the desired hydrocarbons per catalyst mass is higher when using an MFECC bed. As mentioned previously in the introduction section, the single-pass conversion in Multi tubular/PBR is kept at 50% or lower to avoid temperature runaways. The results discussed above prove that the potential of the MFECC bed in minimizing this drawback associated with PBR. The high thermal conductivity of the MFECC bed provided efficient temperature control within the reactor bed, which offers a better opportunity to minimize the selectivity of methane while maximizing the selectivity toward C_{5+} products even at high CO conversions. This is one of the main requirements in industrial applications of FT reactors.
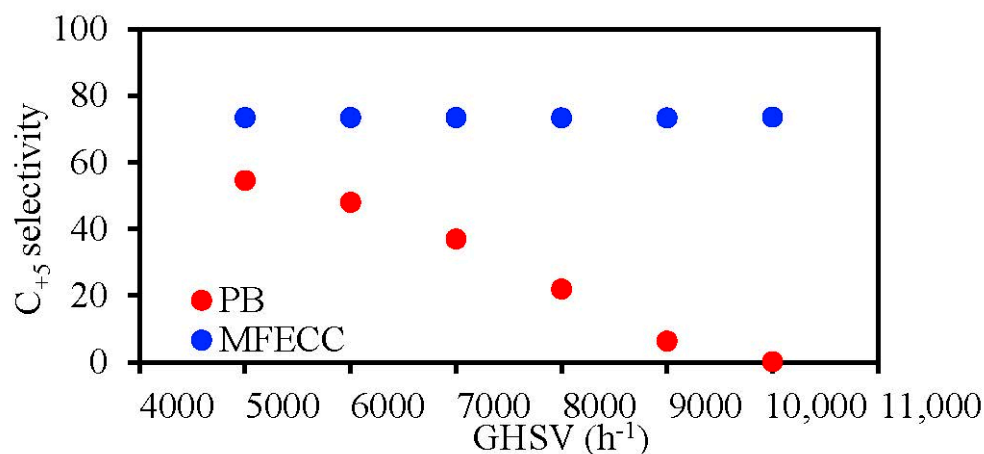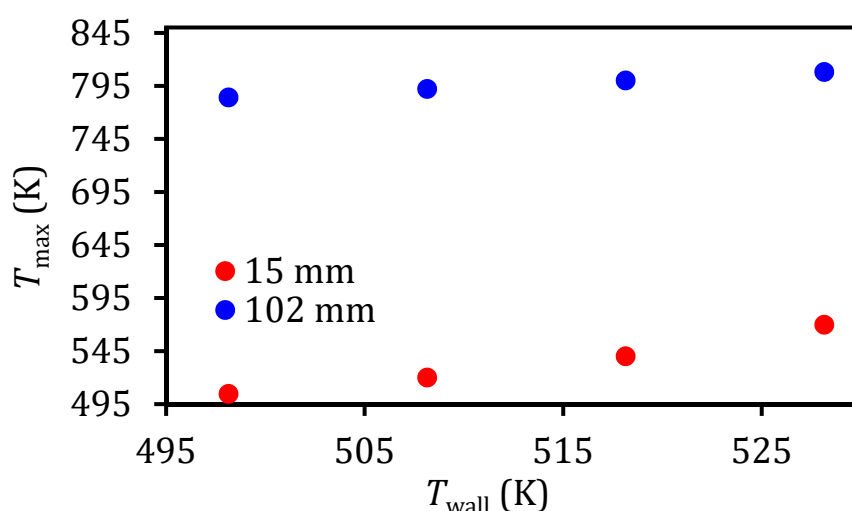

Figure 5. C_{5+} selectivity conversion versus GHSV for PBR and MFECC bed at 528.15 K, 2 MPa pressure, H_2: CO ratio 2:1.
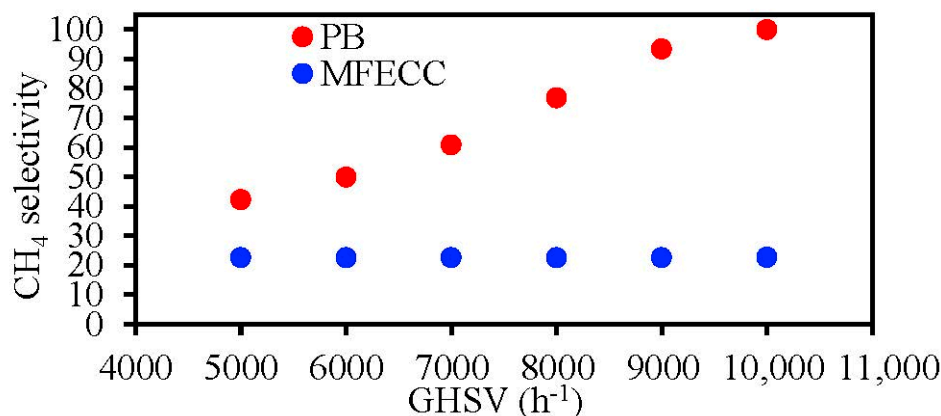

Figure 6. CH_4 selectivity versus GHSV for PBR and MFECC bed at 528.15 K, 2 MPa pressure, H_2: CO ratio 2:1.

### 3.4. Effect of Reactor Tube Size (Scaling-Up)

As mentioned previously, FT is a highly exothermic reaction; thus, efficient heat removal is one of the main considerations while designing commercial-scale FT reactors [7]. Therefore, the range of tube diameters used in industrial-sized PBR reactors is 20 mm to 50 mm. Larger tube sizes provide poor heat management and are more likely to suffer from the local hotspot formation, which results in the formation of methane while lowering the selectivity of the desired C_{5+} hydrocarbon products. For industrial applications, it is important to set up the FT process in a way that would provide high production of higher weight hydrocarbons (C_{5+}), with low methane selectivity and good temperature control within the reactor bed. The results discussed in the previous sections indicate that the latter can be achieved upon utilization of the novel MFECC structures of high thermal conductivity that allows uniformity in temperature distribution across reactor bed at larger tube diameters. Several simulations were performed to study the effect of scaling up the reactor tube diameter up to 102 mm on the thermal behavior of both the PBR and MFECC bed. A comparison between the base case model (15 mm ID) and the scaled-up model (102 mm ID) at 2 MPa pressure and H_2/CO ratio of (2:1) was made at different inlet temperatures 498.15 K to 528.15 K. Since changing the tube diameter affects the gas velocity/GHSV (45-fold reduction in GHSV going from 15 mm up to 102 mm, which has a prominent effect on the mass and heat transport properties), the inlet gas flow rate of the was adjusted to maintain a constant GHSV value of 5000 h^{-1} to provide a fair comparison between the base case and the scaled-up case. Figure 7 shows the maximum temperature rise inside the PBR at various inlet temperatures. If all the process parameters are kept constant, increasing the tube diameter from 15 mm to 102 mm while maintaining constant GHSV (5000 h^{-1}) results in extreme temperature runaway at all inlet temperature conditions, where the hotspot was beyond 200 K. This drastic change in the maximum temperature rise is around 40% to 50% higher than the base case scenario at 15 mm. The extremely high-temperature gradients are mainly due to high radial heat transport resistances at larger tube sizes. As a result of the high temperatures inside the PBR, the CO conversion at 102 mm was beyond 90% at all inlet temperatures, as shown in Figure 8. The reason behind this is that using larger tube diameters accompanied by the use of higher inlet gas flow rates enables higher CO conversions, thus higher hydrocarbon productivity. However, the selectivity toward methane associated with such high-temperature gradients goes up to 100% at all temperature conditions, consequently leading to 0% selectivity toward the desired C_{5+} hydrocarbons, as demonstrated in Figure 9.

Figure 7. Maximum temperature in PBR 102 mm ID with the base case of 15 mm ID at 5000 GHSV, H_2/CO 2:1, 2 MPa pressure.
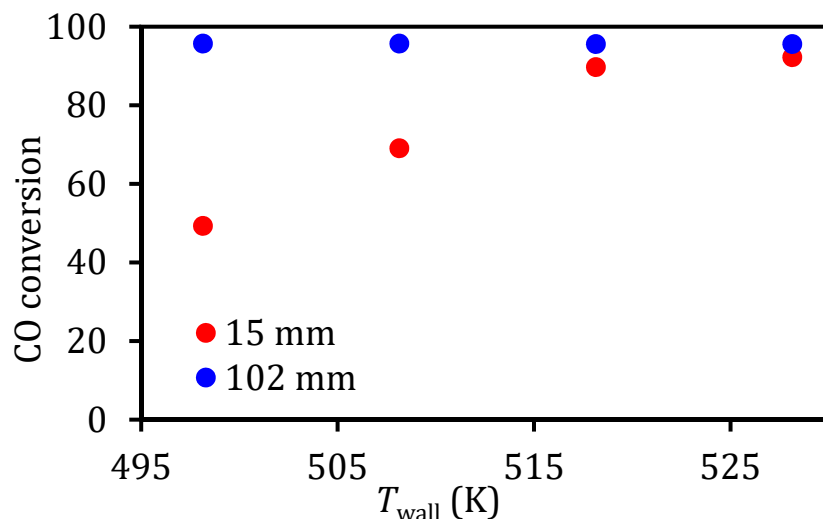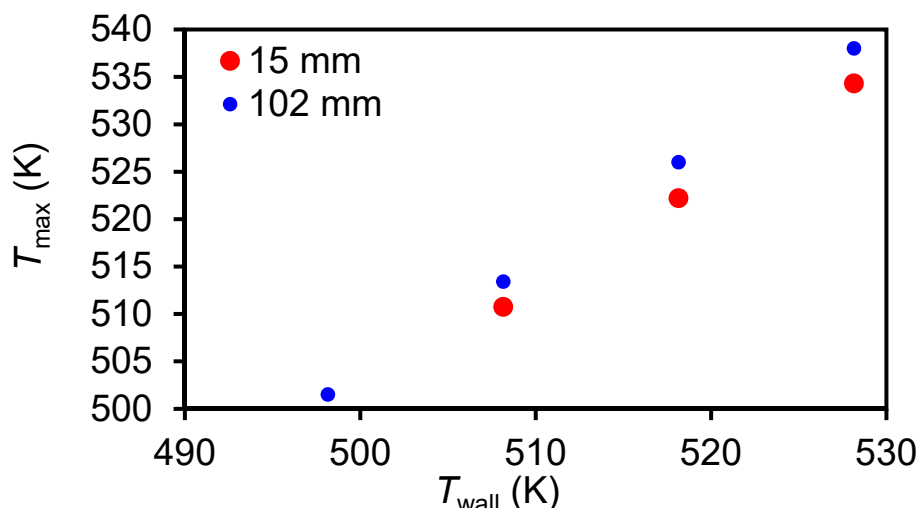
Figure 8. CO conversion in PBR 102 mm ID with the base case of 15 mm ID at 5000 GHSV, H_2/CO 2:1, 2 MPa pressure.
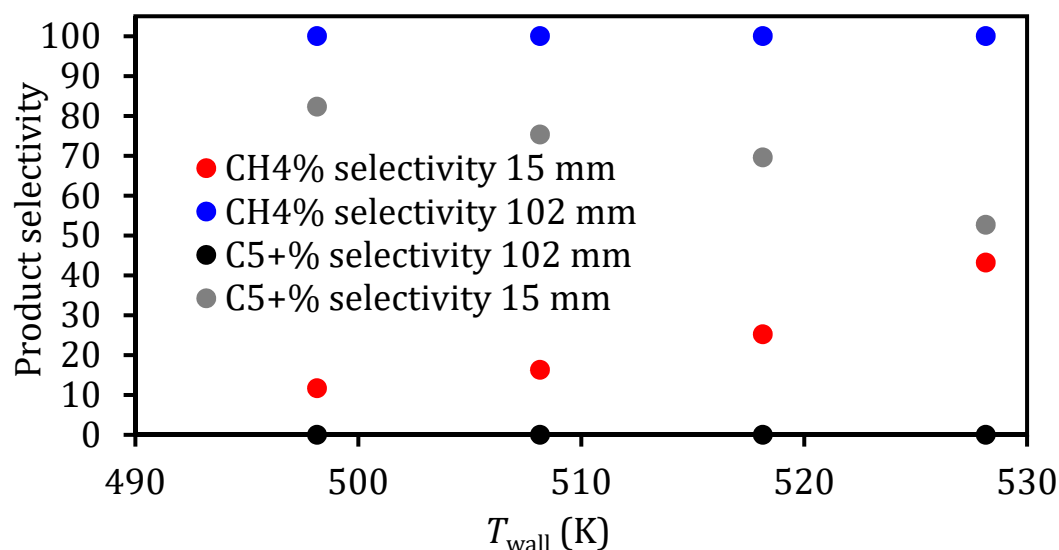

Figure 9. CH_4 and C_{5+} selectivity in PBR 102 mm with the base case of 15 mm ID at 5000 GHSV, H_2/CO 2:1, 2 MPa pressure.

On the other hand, the MFECC bed provided better temperature control relative to the PBR under the same operating conditions when the tube diameter is scaled up to 102 mm. The maximum temperature deviation from the base case (15 mm, 498.15 K to 528.15 K, GHSV 5000 h^{-1}, H_2/CO 2:1, P_{tot} 2 MPa) was below 4 K at all inlet temperature conditions, as shown in Figure 10. This is due to the high radial effective thermal conductivity of the MFECC bed, which was able to facilitate heat removal even at higher radial resistances in larger tubes. Moreover, when the tube diameter is increased from 15 mm to 102 mm while keeping a constant GHSV, the CO conversion goes up by more than 9% for all the simulated temperature conditions, as shown in Figure 11. The latter indicates a noticeable increase in hydrocarbon productivity per tube is achieved for larger tube diameters. An interesting observation is that for 102 mm diameter, the CH_4 selectivity only increases by less than 1.4%, while the C_{5+} decreases by less than 1.3% compared to the base case scenario, as shown in Figure 12. The higher CO conversion, accompanied by selectivity control at 102 mm diameter achieved using the MFECC bed, indicates that higher C_{5+} productivity is obtained relative to the base case.
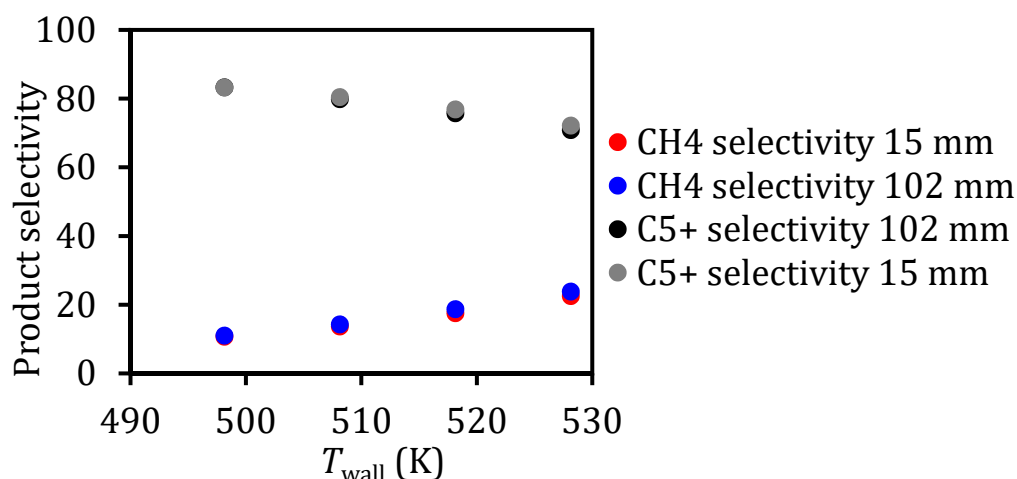
Figure 10. Maximum temperature rise in MFECC 102 mm with the base case of 15 mm ID at 5000 GHSV, H_2/CO 2:1, 2 MPa pressure.
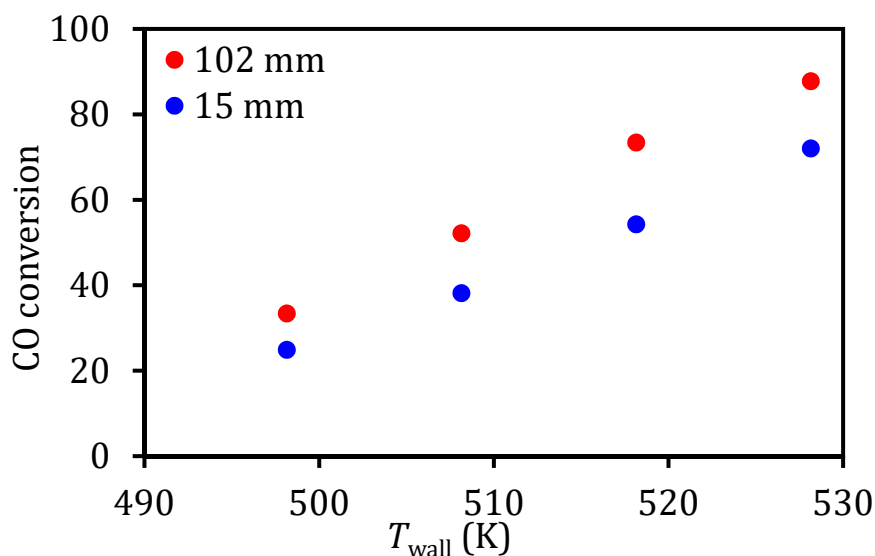
Figure 11. CO conversion in MFECC 102 mm ID with the base case of 15 mm ID at 5000 GHSV, H_2/CO 2:1, 2 MPa pressure.

It is worth noting that, as previously stated that at 528.15 K (only for the case of the PB reactor), the deviation between the modeling and the experimental predictions becomes high. The difference between the maximum temperature (centerline temperature) and the wall temperature is underestimated, thus the model under-predicts the methane selectivity relative to the experimental data. Consequently, the selectivity of C_{5+} products at 528.15 K is over-predicted by the model when compared to experimental data. In the case of scaling up the tube diameter up to 102 mm, for the MFECC case based on the aforementioned discussion, the maximum temperature deviation from the base case (15 mm, 498.15 K to 528.15 K, GHSV 5000 h^{-1}, H_2/CO 2:1, p_{tot} = 2 MPa) was below 4 K at all inlet temperature conditions. Therefore, extremely large temperatures are not observed in this case, hence confirming the reliability of the results for the MFECC bed. In the case of PBR, large temperature deviations are indeed observed (as previously mentioned). However, the selectivity toward methane associated with such high-temperature gradients goes up to 100% at all temperature conditions, consequently leading to 0% selectivity toward the desired C_{5+} hydrocarbons. Although the difference between the maximum temperature (centerline temperature) and the wall temperature is underestimated is this case (methane selectivity should be higher than predicted by the model)

achieving a selectivity beyond 100% is physically not possible. Similarly, for the C_{5+} selectivity, the model over-predicts the C_{5+} selectivity (C_{5+} selectivity should be lower than predicted by the model) and achieving a selectivity below 0% is also physically not possible. The point to be highlighted here is that the hydrocarbon selectivity estimations are very reliable; however, higher temperature gradients are expected when such conditions are practically employed (this will not affect the product selectivity based on the above discussion).

Figure 12. CH_4 and C_{5+} selectivity in MFECC 102 mm ID with the base case of 15 mm ID at 5000 GHSV, H_2/CO 2:1, 2 MPa pressure.

4. Conclusions

A 2D CFD model of an FT reactor was developed in COMSOL® Multiphysics v5.3a for two systems; MFECC bed and conventional PBR under GP-FT conditions. The possibility of scaling-up the reactor diameter tube >15 mm (up to 102 mm ID) was studied as an initial step towards the process intensification of the FT technology. The model results for both the MFECC bed and PBR provided a good match with the experimental predictions for CO conversion, maximum temperature deviation from the wall temperature, CH_4 selectivity, and C_{5+} selectivity. The influence of process parameters (inlet temperature, GHSV, tube diameter) on the hydrocarbon product selectivity, CO conversion, and hotspot formation was investigated. Results indicated that increasing the GHSV from 5000 h^{-1} to 10,000 h^{-1} in the PBR had a detrimental effect on the thermal performance of the reactor bed. This resulted in shifting the product selectivity toward undesired methane (CH_4 selectivity of 100%). Comparing with the MFECC bed simulated under equivalent conditions shows a very small temperature deviation (<7 K) and constant hydrocarbon product selectivity (~22% CH_4 selectivity and ~73% C_{5+} selectivity). Therefore, the near isothermal operation in the MFECC bed facilitates higher C_{5+} hydrocarbon productivities per tube pass at higher space velocities without the risk of selectivity loss. A comparison between the base case model (15 mm ID) and the scaled-up model (102 mm ID) revealed that the high radial effective thermal conductivity of the MFECC bed was able to provide efficient heat removal (temperature gradient < 10 K) even at higher radial distances in larger tubes. In contrast, the PBR suffered from extreme temperature runaways (>200 K), leading to poor product selectivity (100% CH_4 selectivity and 0% C_{5+} selectivity). The ability of the MFECC bed to provide near isothermal operation at 102 mm ID provides a 16-fold reduction in the total number of tubes required to achieve a targeted capacity compared to a conventional 0.025 m ID reactor bed. This study demonstrates the possibility of implementing the MFECC reactor bed in future commercial FT reactors to achieve high production rates by utilizing larger reactor tube diameters.

References

1. Challiwala, M.; Ghouri, M.; Linke, P.; El-Halwagi, M.; Elbashir, N. A combined thermo-kinetic analysis of various methane reforming technologies: Comparison with dry reforming. *J. CO2 Util.* **2017**, *17*, 99111. [CrossRef]

2. Alsuhaibani, A.S.; Afzal, S.; Challiwala, M.; Elbashir, N.O.; El-Halwagi, M.M. The impact of the development of catalyst and reaction system of the methanol synthesis stage on the overall profitability of the entire plant: A techno-economic study. *Catal. Today* **2019**. [CrossRef]

3. Abusrafa, A.E.; Challiwala, M.S.; Choudhury, H.A.; Wilhite, B.A.; Elbashir, N.O. Experimental verification of 2-Dimensional computational fluid dynamics modeling of supercritical fluids Fischer Tropsch reactor bed. *Catal. Today* **2020**, *343*, 165–175. [CrossRef]

4. Elbashir, N.O.; Chatla, A.; Spivey, J.J.; Lemonidou, A. Reaction Engineering and Catalysis Issue in Honor of Professor Dragomir Bukur: Introduction and Review. *Aristotle Univ. Thessalon.* **2020**, *343*, 1–7. [CrossRef]

5. Challiwala, M.S.; Wilhite, B.; Ghouri, M.M.; Elbashir, N. *2-D Modeling of Fischer Tropsch Packed Bed Reactor: First Step Towards Scale-Up*; AIChE: Minneapolis, MN, USA, 2017.

6. Alsuhaibani, A.S.; Afzal, S.; Challiwala, M.; Elbashir, N.O.; El-Halwagi, M.M. Process Systems Engineering and Catalysis: A Collaborative Approach for the Development of Chemical Processes. In *Computer Aided Chemical Engineering*; Muñoz, S.G., Laird, C.D., Realff, M.J., Eds.; Elsevier: Amsterdam, The Netherlands, 2019; pp. 409–414.

7. Dry, M.E. Practical and theoretical aspects of the catalytic Fischer–Tropsch process. *Appl. Catal. A Gen.* **1996**, *138*, 319–344. [CrossRef]

8. Park, N.; Kim, J.-R.; Yoo, Y.; Lee, J.; Park, M.-J. Modeling of a pilot-scale fixed-bed reactor for iron-based Fischer–Tropsch synthesis: Two-Dimensional approach for optimal tube diameter. *Fuel* **2014**, *122*, 229–235. [CrossRef]

9. Challiwala, M.S.; Wilhite, B.A.; Ghouri, M.M.; Elbashir, N.O. Multidimensional modeling of a microfibrous entrapped cobalt catalyst Fischer–Tropsch reactor bed. *AIChE J.* **2017**, *64*, 1723–1731. [CrossRef]

10. Elbashir, N.O.; Challiwala, M.S.; Sengupta, D.; El-Halwagi, M.M. System and Method for Carbon and Syngas Production, World Intellectual Property and Organization. Production, System and Method for Carbon and Syngas. WO Patent 2018187213A1, 11 October 2020.

11. Elbashir, N.; Challiwala, M.S.; Ghouri, M.M.; Linke, P.; El-Halwagi, M. *Modeling Development of a Combined Methane Fixed Bed Reactor Reformer*; Hamad bin Khalifa University Press (HBKU Press): Doha, Qatar, 2016; p. EESP2384.

12. Chatla, A.; Ghouri, M.M.; el Hassan, O.W.; Mohamed, N.; Prakash, A.V.; Elbashir, N.O. An experimental and first principles DFT investigation on the effect of Cu addition to Ni/Al2O3 catalyst for the dry reforming of methane. *Appl. Catal. A Gen.* **2020**, *602*, 117699. [CrossRef]

13. Challiwala, M.S.; Sengupta, D.; El-Halwagi, M.; Elbashir, N. *A Process Integration Approach for a Sustainable Gtl Process Using Tri-Reforming of Methane*; AIChE: Minneapolis, MN, USA, 2017.

14. Challiwala, M.S.; Ghouri, M.M.; Linke, P.; Elbashir, N.O. Kinetic and thermodynamic modelling of methane reforming technologies: Comparison of conventional technologies with dry reforming. In Proceedings of the Conference: Qatar Foundation Annual Research Conference (ARC), Doha, Qatar, 8–13 November 2015.

15. Challiwala, M.S.; Afzal, S.; Choudhury, H.A.; Sengupa, D.; El-Halwagi, M.M.; Elbashir, N.O. Alternative via Pathways Dry Reforming for CO of 2 Utilization Methane. *Adv. Carbon Manag. Technol.* **2020**, *1*, 253.

16.　Omran, A.; Yoon, S.H.; Khan, M.; Ghouri, M.; Chatla, A.; Elbashir, N. Mechanistic Insights for Dry Reforming of Methane on Cu/Ni Bimetallic Catalysts: DFT-Assisted Microkinetic Analysis for Coke Resistance. *Catalysts* **2020**, *10*, 1043. [CrossRef]

17.　Dry, M.E. The fischer-tropsch process: 1950–2000. *Catal. Today* **2002**, *71*, 227–241. [CrossRef]

18.　Filip, L.; Zámostný, P.; Rauch, R. Mathematical model of Fischer-Tropsch synthesis using variable alpha-Parameter to predict product distribution. *Fuel* **2019**, *243*, 603–609. [CrossRef]

19.　Espinoza, R.; Steynberg, A.; Jager, B.; Vosloo, A. Low temperature Fischer-Tropsch synthesis from a Sasol perspective. *Appl. Catal. A Gen.* **1999**, *186*, 13–26. [CrossRef]

20.　Wender, I. Reactions of synthesis gas. *Fuel Process. Technol.* **1996**, *48*, 189–297. [CrossRef]

21.　Todic, B.; Mandic, M.; Nikacevic, N.; Bukur, D.B. Effects of process and design parameters on heat management in fixed bed Fischer-Tropsch synthesis reactor. *Korean J. Chem. Eng.* **2018**, *35*, 875–889. [CrossRef]

22.　Steynberg, A.; Espinoza, R.; Jager, B.; Vosloo, A. High temperature Fischer–Tropsch synthesis in commercial practice. *Appl. Catal. A Gen.* **1999**, *186*, 41–54. [CrossRef]

23.　Yang, J.H.; Kim, H.-J.; Chun, D.H.; Lee, H.-T.; Hong, J.-C.; Jung, H.; Yang, J.-I. Mass transfer limitations on fixed—Bed reactor for Fischer-Tropsch synthesis. *Fuel Process. Technol.* **2010**, *91*, 285–289. [CrossRef]

24.　Fratalocchi, L.; Visconti, C.G.; Groppi, G.; Lietti, L.; Tronconi, E. Intensifying heat transfer in Fischer-Tropsch tubular reactors through the adoption of conductive packed foams. *Chem. Eng. J.* **2018**, *349*, 829–837. [CrossRef]

25.　Mandić, M.; Todić, B.; Živanić, L.; Nikačević, N.; Bukur, D.B. Effects of Catalyst Activity, Particle Size and Shape, and Process Conditions on Catalyst Effectiveness and Methane Selectivity for Fischer-Tropsch Reaction: A Modeling Study. *Ind. Eng. Chem. Res.* **2017**, *56*, 2733–2745. [CrossRef]

26.　Sie, S.; Krishna, R. Fundamentals and selection of advanced Fischer–Tropsch reactors. *Appl. Catal. A Gen.* **1999**, *186*, 55–70. [CrossRef]

27.　Botes, F.; Niemantsverdriet, J.; Van De Loosdrecht, J. A comparison of cobalt and iron based slurry phase Fischer–Tropsch synthesis. *Catal. Today* **2013**, *215*, 112–120. [CrossRef]

28.　Lu, X. Fischer-Tropsch Synthesis: Towards Understanding. 2011. Available online: http://hdl.handle.net/10539/11175 (accessed on 27 September 2020).

29.　Sheng, M.; Yang, H.; Cahela, D.R.; Tatarchuk, B. Novel catalyst structures with enhanced heat transfer characteristics. *J. Catal.* **2011**, *281*, 254–262. [CrossRef]

30.　Sheng, M.; Yang, H.; Cahela, D.R.; Yantz, W.R., Jr.; Gonzalez, C.F.; Tatarchuk, B.J. High conductivity catalyst structures for applications in exothermic reactions. *Appl. Catal. A Gen.* **2012**, *445*, 143–152. [CrossRef]

31.　Sheng, M.; Cahela, D.R.; Yang, H.; Gonzalez, C.F.; Yantz, W.R.; Harris, D.K.; Tatarchuk, B. Effective thermal conductivity and junction factor for sintered microfibrous materials. *Int. J. Heat Mass Transf.* **2013**, *56*, 10–19. [CrossRef]

32.　Kalluri, R.R.; Cahela, D.R.; Tatarchuk, B. Microfibrous entrapped small particle adsorbents for high efficiency heterogeneous contacting. *Sep. Purif. Technol.* **2008**, *62*, 304–316. [CrossRef]

33.　Yang, H.; Cahela, D.R.; Tatarchuk, B. A study of kinetic effects due to using microfibrous entrapped zinc oxide sorbents for hydrogen sulfide removal. *Chem. Eng. Sci.* **2008**, *63*, 2707–2716. [CrossRef]

34.　Zhu, W.H.; Flanzer, M.E.; Tatarchuk, B. Nickel–zinc accordion-fold batteries with microfibrous electrodes using a papermaking process. *J. Power Sources* **2002**, *112*, 353–366. [CrossRef]

35.　Greiner, A.; Wendorff, J.H. Electrospinning: A fascinating method for the preparation of ultrathin fibers. *Angew. Chem. Int. Ed.* **2007**, *46*, 5670–5703. [CrossRef]

36.　Le Bars, M.; Worster, M.G. Interfacial conditions between a pure fluid and a porous medium: Implications for binary alloy solidification. *J. Fluid Mech.* **2006**, *550*, 149–173. [CrossRef]

37.　Nield, D. The limitations of the Brinkman-Forchheimer equation in modeling flow in a saturated porous medium and at an interface. *Int. J. Heat Fluid Flow* **1991**, *12*, 269–272. [CrossRef]

38.　Hicks, R.E. Pressure Drop in Packed Beds of Spheres. *Ind. Eng. Chem. Fundam.* **1970**, *9*, 500–502. [CrossRef]

39.　Fuller, E.N.; Schettler, P.D.; Giddings, J.C. New method for prediction of binary gas-phase diffusion coefficients. *Ind. Eng. Chem.* **1966**, *58*, 18–27. [CrossRef]

40.　Chabot, G.; Guilet, R.; Cognet, P.; Gourdon, C. A mathematical modeling of catalytic milli-fixed bed reactor for Fischer–Tropsch synthesis: Influence of tube diameter on Fischer Tropsch selectivity and thermal behavior. *Chem. Eng. Sci.* **2015**, *127*, 72–83. [CrossRef]

41. Ghouri, M.; Afzal, S.; Hussain, R.; Blank, J.; Bukur, D.B.; Elbashir, N. Multi-scale modeling of fixed-bed Fischer Tropsch reactor. *Comput. Chem. Eng.* **2016**, *91*, 38–48. [CrossRef]

42. Mamonov, N.A.; Kustov, L.; Alkhimov, S.A.; Mikhailov, M.N. One-dimensional heterogeneous model of a Fischer-Tropsch synthesis reactor with a fixed catalyst bed in the isothermal granules approximation. *Catal. Ind.* **2013**, *5*, 223–231. [CrossRef]

43. Bunnell, D.G.; Irvin, H.B.; Olson, R.W.; Smith, J.M. Effective Thermal Conductivities in Gas-Solid Systems. *Ind. Eng. Chem.* **1949**, *41*, 1977–1981. [CrossRef]

44. Campbell, J.; Huntington, R. Part II, Heat Transfer and Temperature Gradients. *Pet. Refin.* **1952**, *31*, 123–131.

45. De Wasch, A.; Froment, G. Heat transfer in packed beds. *Chem. Eng. Sci.* **1972**, *27*, 567–576. [CrossRef]

46. Specchia, V.; Baldi, G.; Sicardi, S. Heat transfer in packed bed reactors with one phase flow. *Chem. Eng. Commun.* **1980**, *4*, 361–380. [CrossRef]

47. Bauer, R. Effective radial thermal conductivity of packings in gas flow. *Int. Chem. Eng.* **1978**, *18*, 181–204.

48. Dixon, A.G. Wall and particle-shape effects on heat transfer in packed beds. *Chem. Eng. Commun.* **1988**, *71*, 217–237. [CrossRef]

49. Specchia, V.; Sicardi, S. Modified correlation for the conductive contribution of thermal conductivity in packed bed reactors. *Chem. Eng. Commun.* **1980**, *6*, 131–139. [CrossRef]

50. Plautz, D.A.; Johnstone, H.F. Heat and mass transfer in packed beds. *AIChE J.* **1955**, *1*, 193–199. [CrossRef]

51. Quinton, J.; Storrow, J.A. Heat transfer to air flowing through packed tubes. *Chem. Eng. Sci.* **1956**, *5*, 245–257. [CrossRef]

52. Kunii, D.; Smith, J.M. Heat transfer characteristics of porous rocks. *AIChE J.* **1960**, *6*, 71–78. [CrossRef]

53. Yates, I.C.; Satterfield, C.N. Intrinsic kinetics of the Fischer-Tropsch synthesis on a cobalt catalyst. *Energy Fuels* **1991**, *5*, 168–173. [CrossRef]

54. Vervloet, D.; Kapteijn, F.; Nijenhuis, J.; Van Ommen, J.R. Fischer-Tropsch reaction–diffusion in a cobalt catalyst particle: Aspects of activity and selectivity for a variable chain growth probability. *Catal. Sci. Technol.* **2012**, *2*, 1221–1233. [CrossRef]

55. Stamenic, M.; Dikić, V.; Mandić, M.; Todić, B.; Bukur, D.B.; Nikačević, N.M. Multiscale and Multiphase Model of Fixed Bed Reactors for Fischer-Tropsch Synthesis: Intensification Possibilities Study. *Ind. Eng. Chem. Res.* **2017**, *56*, 9964–9979. [CrossRef]

56. Bukur, D.B.; Mandić, M.; Todic, B.; Nikačević, N.M. Pore diffusion effects on catalyst effectiveness and selectivity of cobalt based Fischer-Tropsch catalyst. *Catal. Today* **2020**, *343*, 146–155. [CrossRef]

57. Maretto, C.; Krishna, R. Design and optimisation of a multi-stage bubble column slurry reactor for Fischer–Tropsch synthesis. *Catal. Today* **2001**, *66*, 241–248. [CrossRef]

58. Ma, W.; Jacobs, G.; Das, T.K.; Masuku, C.M.; Kang, J.; Pendyala, V.R.R.; Crocker, M.; Klettlinger, J.L.S.; Yen, C.H. Fischer–Tropsch Synthesis: Kinetics and Water Effect on Methane Formation over 25%Co/γ-Al$_2$O$_3$ Catalyst. *Ind. Eng. Chem. Res.* **2014**, *53*, 2157–2166. [CrossRef]

59. Todic, B.; Bhatelia, T.J.; Froment, G.F.; Ma, W.; Jacobs, G.; Davis, B.H.; Bukur, D.B. Kinetic Model of Fischer–Tropsch Synthesis in a Slurry Reactor on Co-Re/Al2O3 Catalyst. *Ind. Eng. Chem. Res.* **2013**, *52*, 669–679. [CrossRef]

60. Chernobaev, I.; Yakubovich, M.; Tripol'skii, A.; Pavlenko, N.; Struzhko, V. Investigation of the mechanism of methane formation in the fischer-tropsch synthesis on a Co/SiO$_2$ Zr IV catalyst. *Theor. Exp. Chem.* **1997**, *33*, 38–40. [CrossRef]

61. Lee, W.; Bartholomew, C.H. Multiple reaction states in CO hydrogenation on alumina-supported cobalt catalysts. *J. Catal.* **1989**, *120*, 256–271. [CrossRef]

62. Sheng, M.; Gonzalez, C.F.; Yantz, W.R.; Cahela, D.R.; Yang, H.; Harris, D.R.; Tatarchuk, B. Micro Scale Heat Transfer Comparison between Packed Beds and Microfibrous Entrapped Catalysts. *Eng. Appl. Comput. Fluid Mech.* **2013**, *7*, 471–485. [CrossRef]